PLOS ONE

RESEARCH ARTICLE

Influence of sugar concentration on the vesicle compactness, deformation and membrane poration induced by anionic nanoparticles

Sharif Hasan[1], Mohammad Abu Sayem Karal[1]*, Salma Akter[1], Marzuk Ahmed[1], Md. Kabir Ahamed[1,2], Shareef Ahammed[1]

1 Department of Physics, Bangladesh University of Engineering and Technology, Dhaka, Bangladesh,
2 Radiation, Transport and Waste Safety Division, Bangladesh Atomic Energy Regulatory Authority, Dhaka, Bangladesh

* asayem221@phy.buet.ac.bd

Abstract

Sugar plays a vital role in the structural and functional characteristics of cells. Hence, the interaction of NPs with cell membranes in the presence of sugar concentrations is important for medicinal and pharmacological innovations. This study integrated three tools: giant unilamellar vesicles (GUVs), anionic magnetite nanoparticles (NPs), and sugar concentrations, to understand a simplified mechanism for interactions between the vesicle membranes and NPs under various sugar concentrations. We focused on changing the sugar concentration in aqueous solution; more precisely, sucrose inside the GUVs and glucose outside with equal osmolarity. 1,2-dioleoyl-*sn*-glycero-3-phospho-(1′-*rac*-glycerol) (sodium salt) (DOPG) and 1,2-dioleoyl-*sn*-glycero-3-phosphocholine (DOPC) were used to prepare the charged membranes of 40mole%DOPG/60mole%DOPC-GUVs, whereas only DOPC was used to prepare the neutral membranes. Phase contrast fluorescence microscopy shows that the adherence of 18 nm magnetite NPs with anionic charge depends on the sugar concentration. The alterations of GUVs induced by the NPs are characterized in terms of i) vesicle compactness, ii) deformation, and iii) membrane poration. The presence of sugar provides additional structural stability to the GUVs and reduces the effects of the NPs with respect to these parameters; more precisely, the higher the sugar concentration, the smaller the alteration induced by the NPs. The differences in NPs effects are explained by the change in the type of interaction between sugar molecules and lipid membranes, namely enthalpy and entropy-driven interaction, respectively. In addition, such alterations are influenced by the surface charge density of the lipid bilayer. The surface pressure of membranes due to the adsorption of NPs is responsible for inducing the poration in membranes. The differences in deformation and poration in charged and neutral GUVs under various sugar concentrations are discussed based on the structure of the head of lipid molecules.

Competing interests: The authors have declared that no competing interests exist.

1. Introduction

Nanoparticles (NPs) of sizes less than 100 nm have been used in several biomedical applications such as cellular imaging [1], gene delivery [2], cancer treatment [3, 4], and targeted drug delivery [5–7]. In contrast, such NPs show antibacterial and anticarcinogenic properties [8–13] along with cytotoxic effects [14]. The adverse effect of NPs on human health occurs due to the entry of NPs into the body from environmental pollutants [15–19], medical implants, MRI contrast agents, insecticides, and food product processing particles [20–22], resulting in the discomfort of the cardiovascular and respiratory systems [23, 24]. One of the main reasons for this discomfort is the interaction of NPs with biomembranes and the changes in their biophysical and biochemical properties [25–27]. Magnetite NPs can be found from burning fuel in the iron industry, printer toners, stoves, etc. Plenty of magnetite NPs were identified in the human brain, which are prolific in urban areas. The presence of magnetite NPs in the brain causes neurodegenerative diseases such as Alzheimer's [28, 29]. As previously stated, NPs interact with cell membranes, and thus the stability of the membranes in aqueous solution is influenced by various ingredients such as salt concentration and lipid bilayer surface charge density [30]. Sugar, in addition to these elements, plays an important role in the structural and functional properties of biomembranes under various conditions [31–33]. In addition to its critical role in cellular regulation, it has a wide range of applications in medical and industrial research [34, 35]. Sugar influences the spontaneous curvature of vesicles [36], specific capacitance of membranes [37], and bending rigidity of membranes [38–40]. Recently, we investigated the effects of sugar concentration on electroporation in lipid vesicles for the possible application of electroporation technology in cancer/tumor ablation [41]. Therefore, a better understanding of how NPs interact with cells in the presence of various sugar concentrations is vital for medicinal and pharmacological inventions. Cell-sized giant unilamellar vesicles (GUVs) have been used to investigate the interaction of membrane active agents (e.g., peptides, toxins) with lipid membranes [42–45]. GUVs have also been used to study the formation of pores using mechanical tension and electric field [46, 47].

The bending rigidity of lipid membranes changes with sugar concentration [38, 40]. Sugar molecules strongly interacted with the lipid membranes and inserted between the head group of phospholipids at relatively lower sugar concentrations [48]. This insertion lowered the lipid head group area by increasing the surface pressure. In the aqueous phase, a portion of the carbohydrate molecules accumulates in the membrane, forming a kind of additive [36, 49].

At lower sugar concentrations, an enthalpy-driven attractive interaction between sugars and the lipid head group was considered, while at higher sugar concentrations, an entropy-driven repulsive interaction was considered [50, 51].

There is a debate about transporting NPs into mammalian cells. NPs have entered using endocytosis pathway inhibitors [52], but the situation is not entirely obvious for erythrocytes [53]. The interaction of NPs with membranes involves hydrophobic mismatch effects [54], chain stretching of the lipids near the site of interaction [55], spontaneous curvature of membranes [56], changes in lipid packing [57], and pearling [58]. Various aspects of the interaction of NPs with lipid membranes were considered [59]. Magnetic NPs with a cationic core-shell tended to bind to positively charged bilayers [60]. Shape change (protrusion, pearling) of neutral GUVs was observed in the presence of encapsulating cationic NPs [58]. Membrane deformation occurs due to the binding of NPs with membranes [60, 61]. Recently, the interaction of anionic magnetic NPs (same as used here) with charged and neutral membranes in the presence of a fixed sugar concentration has been investigated [30], in which the interaction of NPs is explained based on the key role of the dipoles of DOPC lipids. As previously stated, sugar plays an important role in the structural and functional aspects of the lipid bilayer; thus, the

question arises how sugar influences the NPs-induced vesicle compactness, vesicle deformation, and lipid membrane poration. These are the main goals of this investigation. As phosphocholine (PC) lipids are available in human cells, both charged and neutral vesicles prepared by PC membranes have been considered for quantification of compactness, fraction of deformed GUVs, and fraction of pore formed GUVs.

2. Materials and methods

2.1 Chemicals and reagents

Negatively charged lipid 1,2-dioleoyl-*sn*-glycero-3-phospho-(1′-*rac*-glycerol) (sodium salt) (DOPG) and neutral lipid 1,2-dioleoyl-*sn*-glycero-3-phosphocholine (DOPC) were purchased from Avanti Polar Lipids Inc. (Alabaster, AL). Bovine serum albumin (BSA), Piperazine-1, 4-bis (2-ethanesulfonic acid) (PIPES), O,O′-Bis (2-aminoethyl) ethyleneglycol-*N,N,N′,N′*,-tetraacetic acid (EGTA) were purchased from Sigma-Aldrich (Germany). Ferric chloride anhydrous ($FeCl_3$), ferrous chloride tetra hydrate ($FeCl_2 \cdot 4H_2O$), sucrose, and glucose were purchased from Merck, Germany.

2.2 Ipomoea aquatica leaf extracts mediated NPs

The green synthesis method was used to synthesize the NPs with a size of 18 nm as reported in our previous paper [62]. The synthesized particles had a cubic inverse spinel type phase. The zeta potential of the NPs was obtained at −21.3 mV [30]. *Ipomoea aquatica* (widely known as water spinach) was bought from Palashi market, Dhaka, Bangladesh. It is also available in any market in Bangladesh. At first, 60 g *Ipomoea aquatica* leaves paste was mixed into 400 mL deionized water and heated at 80˚C for 4 hours at 800 rpm. 20 mL of 0.05 M $FeCl_2 \cdot 4H_2O$ and 20 mL of 0.10 M $FeCl_3$ were mixed together at 60˚C using 800 rpm and after 10 min, 5 mL leaf extract was added into the mixture, and after another 10 min 100 mL of 0.10 M NaOH solution was added to the mixture. During addition of NaOH, the nanoparticles were formed in the colloidal solution. The biomolecules of leaf extracts acted as stabilizers as well as reducing agents to prepare NPs using $FeCl_3$ and $FeCl_2 \cdot 4H_2O$ as precursors.

The NPs were accumulated at the bottom of the glass beaker using a bar magnet, and the upper solution of NPs was discarded. The collected NPs were kept in a drier at 60˚C for 2–3 days for fine drying. We prepared fine powders from dried NPs using a hand mortar. A higher concentration (0.20 mg/mL) of NPs was prepared in buffer (for charged membranes) or in MilliQ (for neutral membranes), which was then diluted to prepare 0.006, 0.01, and 0.013 mg/mL NPs solutions. The 100 μL NPs were then mixed with 200 μL suspension of purified GUVs in a microchamber (total 300 μL) for interacting the NPs with membranes. Hence, the corresponding effective NPs concentrations in the chamber were 2.00, 3.33, and 4.67 μg/mL.

2.3 Synthesis of lipid membranes of GUVs

Among the various methods to prepare the GUVs [63], we followed the well-known natural swelling method [64]. Charged membranes of 40%DOPG/60%DOPC-GUVs (where % indicates mole %) and neutral membranes of 100%DOPC-GUVs (i.e., DOPC-GUVs) with 1 mM concentration of DOPG and DOPC lipids (total volume 200 μL) were taken into a 4.5 mL glass vial individually. The samples were dried with a gentle flow of nitrogen gas to produce a thin, homogeneous lipid film. The vials were then kept in a vacuum desiccator for 12 hours. 20 μL MilliQ water was added into the vial for pre-hydration at 45˚C for 8 min. The 40%DOPG/60% DOPC-GUVs and DOPC-GUVs were incubated for 3.0 hours at 37˚C with 1 mL PIPES buffer (10 mM PIPES, 150 mM NaCl, pH 7.0, 1mM EGTA) and MilliQ water containing various

concentrations of sucrose, respectively. Using these procedures, a population of charged and neutral GUVs were formed, which contained various concentrations of sucrose solution inside. To prepare the fluorescent probe (calcein) encapsulated GUVs, we used 1 mM calcein with various concentrations of sucrose in buffer (for charged vesicles) and MilliQ (for neutral vesicles) for incubation of the suspension of vesicles. Membrane filtering method was used to get the purified suspension of GUVs [65, 66] with outside solution of 40%DOPG/60%DOPC-GUVs and DOPC-GUVs were PIPES buffer and MilliQ containing various concentrations of glucose, respectively. Four different concentrations of sugar, i.e., c = 50, 100, 200 and 300 mM were used in these investigations. The concentration values refer to the concentrations of both sucrose (inside the GUV) and glucose (outside the GUV), which were kept equal to avoid any osmotic effect. After purification, 200 μL purified GUVs suspension was taken into a micro-chamber of volume 300 μL and then 100 μL NPs was added into the suspension. The effective NPs concentrations in the microchamber were 2.00, 3.33, and 4.67 μg/mL. The microchamber was prepared by inserting a U-shaped silicone rubber spacer onto a glass slide. We did not measure the concentration of GUVs but measured NPs concentrations. To remove the strong attraction between the glass surface and the membranes, the microchamber and the glass surface were coated with 0.10% (w/v) BSA solution. An inverted phase contrast fluorescent microscope (Olympus IX-73, Japan) with a 20× objective at 25 ± 1˚C was used to observe the GUVs. The images were recorded using a charge-coupled device (CCD) camera (Olympus DP22, Japan) with a recording speed of 25 frames per second. The size of GUVs was measured using the cellSens Dimension (Ver. 3.2) PC software (Olympus Corporation, Japan).

2.4 NPs-induced compactness of GUVs

To investigate the NPs-induced compactness (C_{om}) of GUVs, 100 μL NPs was added to 200 μL purified GUVs. We focused a GUV during the NPs interaction. The dynamics of that GUV was recorded using a charge-coupled device camera connected with phase contrast mode in the microscope. The time-dependent compactness and sugar concentration-dependent compactness for charged and neutral GUVs were determined. Compactness quantifies the change of the shape of GUVs [67] that can be directly measured using appropriate software. MATLAB image processing toolbox was used to calculate the C_{om} for each deformed image. The compactness is defined as follows [30]:

$$C_{om} = \frac{P^2}{4\pi S_{cr}} \tag{1}$$

where P is the perimeter and S_{cr} is the image cross section area of a GUV. The minimal value of C_{om} is equal to 1.0 for a perfect circle while its value increases with any deviation. The degree of deformation of a GUV is determined by the value of compactness.

2.5 NPs-induced fraction of deformed GUVs and fraction of pore formed GUVs

The fraction of deformed GUVs (Fr_d) and the fraction of pore formed GUVs (Fr_p) were calculated by measuring the probability of deformation and poration among all the measured GUVs. Here, we explain how to calculate these fractions. 100 μL NPs were interacted with 200 μL purified GUVs suspension. During interaction of NPs with GUVs, the images of vesicles were taken at time 0, 10, 20, 30, 40, 50 and 60 min by keeping the focus at a fixed position. Then, similar experiments were done for 2nd and 3rd chambers. The number of deformed GUVs and pore formed GUVs were calculated among all the examined GUVs from several images in each time. We calculated the Fr_d and Fr_p at different times for an independent

experiment. Pore-formed GUVs mean GUVs that have formed pores in their membranes by NPs. The same procedure was performed for 3 independent experiments, and the values of Fr_d and Fr_p for each independent experiment were obtained. The sugar concentration-dependent average value with standard deviation of Fr_d and Fr_p were calculated at each defined time.

2.6 NPs-induced leakage of encapsulating calcein of GUVs

To investigate the NPs-induced leakage of encapsulating calcein of GUVs, 100 μL NPs were added to calcein encapsulated GUVs suspension of 200 μL in a microchamber. We focused on a 'single GUV' during interaction. The GUV was recorded using a CCD camera connected with fluorescence mode in a microscope. The starting time of pore formation in the membranes of GUVs occurred when the leakage of calcein started to decrease rapidly. The time-dependent leakage of several GUVs was observed for various sugar concentrations.

3. Results

3.1 Deformation and compactness of 40%DOPG/60%DOPC-GUVs and DOPC-GUVs induced by 3.33 μg/mL NPs in presence of various sugar concentrations

At first, we investigated the magnetite NPs-induced deformation of 40%DOPG/60%DOPC-GUVs and DOPC-GUVs induced by 3.33 μg/mL NPs. To measure the degree of deformation of a GUV, the corresponding compactness (C_{om}) was determined. The phase contrast images of the dynamic change of a 40%DOPG/60%DOPC-GUV due to the interaction of 3.33 μg/mL NPs under 50 mM sugar concentration is presented in Fig 1(A). The similar experimental results for DOPC-GUVs under the same condition is presented in Fig 1(B). Before addition of NPs into the suspension of GUVs at 50 mM sugar concentration, the vesicles were perfectly spherical in shape as shown in Fig 1(A) and 1(B) at 0 min. As the time progressed, the vesicles started to deform from their spherical shape, and the deformation was observed to increase with time. At 0 min (before interacting the NPs), the value of C_{om} was 1.0 for both GUVs, and it increased with time after interacting with NPs. In Fig 1(A), the values of C_{om} were 1.05, 1.12, 1.19, 1.28, and 1.34 at 13, 25, 33, 50 and 60 min, respectively. For neutral GUVs, the values of C_{om} were 1.07, 1.13, 1.20, 1.25 and 1.30 at 15, 30, 42, 50 and 60 min, respectively as shown in Fig 1(B). The time-dependent change of C_{om} of Fig 1(A) and 1(B) are presented in Fig 1(C) and 1(F), respectively. The C_{om} increases with time for both GUVs. These deformations were similar to those observed before in our experiment for a fixed sugar concentration [30]. Similar experiments were conducted for many GUVs (number of measured GUVs, N = 15) to confirm the reproducibility. To compare the compactness of different GUVs, the time course of the change in C_{om} of 10 'single 40%DOPG/60%DOPC-GUVs' in an independent experiment at 50 mM sugar concentration is shown in Fig 1(D). These results clearly indicate that when NPs are adsorbed into the membrane of GUVs, the vesicles became deformed. The deformation of GUVs for three other sugar concentrations was also investigated, namely, c = 100, 200 and 300 mM, and then the corresponding C_{om} values were measured.

It is necessary to explain how to calculate the average compactness, C_{om}^{av}. For example, in the first experiment, the value of mean compactness at time 30 min was 1.150 for 15 different GUVs (N = 15) under c = 50 mM. The values of mean compactness at time 30 min were 1.142 for N = 17 and 1.149 for N = 18, respectively in the second and third experiments under the same sugar concentration. Therefore, the C_{om}^{av} at 30 min for 3 independent experiments (number of independent experiment, n = 3) was (1.150 + 1.142 + 1.149)/3 using N = 15–18 under c = 50 mM. C_{om}^{av} for other times were also measured under the same conditions.
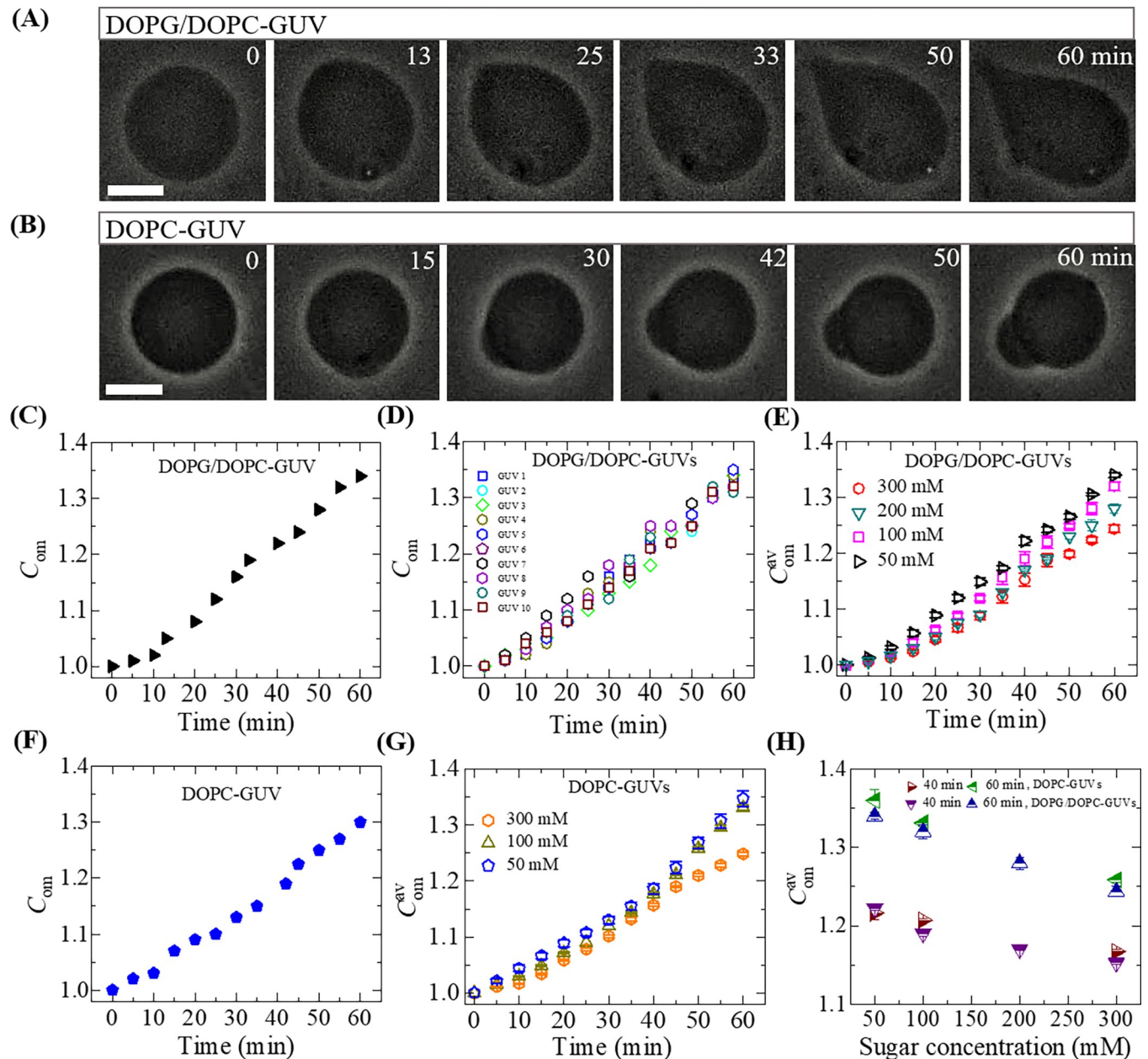
Fig 1. The deformation and compactness of charged and neutral GUVs induced by 3.33 μg/mL NPs. Phase contrast images show the deformation of a (A) 40%DOPG/60%DOPC-GUV and (B) DOPC-GUV in the presence of 50 mM sugar concentration. The numbers on each image indicate the time in minute after addition of NPs. Scale bar is 15 μm. The time course of the change in C_{om} of (C) 40%DOPG/60%DOPC-GUV and (F) DOPC-GUV as shown in (A) and (B), respectively. (D) The time course of the change in C_{om} of 10 'single 40%DOPG/60%DOPC-GUVs' in an independent experiment at 50 mM sugar concentration. The time course of average compactness (C_{om}^{av}) of many (E) 40%DOPG/60%DOPC-GUVs and (G) DOPC-GUVs at c = 50, 100, 200 and 300 mM. (H) The sugar concentration-dependent C_{om}^{av} at different times for 40%DOPG/60%DOPC and DOPC-GUVs. Average values with standard deviations of C_{om} were determined from 3 independent experiments using 15–18 GUVs in each independent experiment.

The change in C_{om}^{av} with time for different sugar concentrations is shown in Fig 1(E) for charged 40%DOPG/60%DOPC-GUVs and in Fig 1(G) for neutral DOPC-GUVs. In Fig 1(E) and 1(G), it is clearly observed that the rate of increment of C_{om}^{av} with time is different for different sugar conditions. We also calculated the sugar concentration-dependent C_{om}^{av}. Fig 1(H) shows the sugar concentration-dependent C_{om}^{av} for both charged and neutral GUVs,

respectively, in which the C_{om}^{av} decreased with the increase of sugar concentration. As for example, the value of C_{om}^{av} was (1.22 ± 0.01) for c = 50 mM and (1.15 ± 0.01) for c = 300 mM at 40 min for 40%DOPG/60%DOPC-GUVs. Additionally, the value of C_{om}^{av} was (1.35 ± 0.01) for c = 50 mM and (1.25 ± 0.01) for c = 300 mM at 60 min for DOPC-GUVs. These investigations suggested that higher concentrations of sugar inhibited the deformation of lipid vesicles.

3.2 Fraction of deformed 40%DOPG/60%DOPC-GUVs induced by 3.33 μg/mL NPs under various sugar concentrations

In section 3.1, we studied the NPs-induced deformation of an individual GUV and their corresponding C_{om}. Now, we describe the interaction of 3.33 μg/mL NPs on the ensemble of 40% DOPG/60%DOPC-GUVs under various concentrations of sugar. Addition of NPs into the suspension of vesicles deformed some GUVs, pore formed some GUVs, and some GUVs remain unchanged. Let us explain how to calculate the fraction of deformed GUVs (Fr_d) at different time. In this regard, after addition of NPs into the GUVs suspension in the microchamber, images of GUVs were taken at 0, 10, 20, 30, 40, 50, and 60 min without changing the microscope focusing position. Similar experiments were done for second and third chamber. Next, we counted the number of deformed GUVs among all the examined GUVs (N = 15−20) from several phase contrast images at time 0, 10, 20, 30, 40, 50 and 60, min. Deformed GUVs mean GUVs that have deformed by NPs. In the first independent experiment, if 50 GUVs were counted from several images from where 10 GUVs were deformed at 20 min after mixing the NPs, the value of Fr_d = 0.20 at that time. We calculated the Fr_d for different times. We considered these investigations as independent experiments. The values of Fr_d for 40%DOPG/ 60%DOPC-GUVs at time 0, 10, 20, 30, 40, 50, and 60 min were obtained 0, 0.10, 0.18, 0.22, 0.30, 0.32, and 0.40, respectively, under c = 200 mM. These data confirmed that Fr_d increased with time. We followed the similar procedure as described above for 3 times (n = 3). The average value with standard deviation of Fr_d obtained from those independent experiments for c = 200 mM with time is shown in Fig 2(A). The average values of Fr_d at 0, 10, 20, 30, 40, 50 and 60 min were obtained 0, (0.11 ± 0.01), (0.16 ± 0.01), (0.21 ± 0.01), (0.28 ± 0.01), (0.33 ± 0.02) and (0.40 ± 0.02), respectively (Fig 2A). The average value of Fr_d also increased with time. We carried out the similar type of experiments for a variety of sugar concentrations, such as 50, 100, 200 and 300 mM. The time-dependent bar diagram for the average Fr_d at 3.33 μg/mL under various sugar concentrations is shown in Fig 2(B). At 40 min, the values of
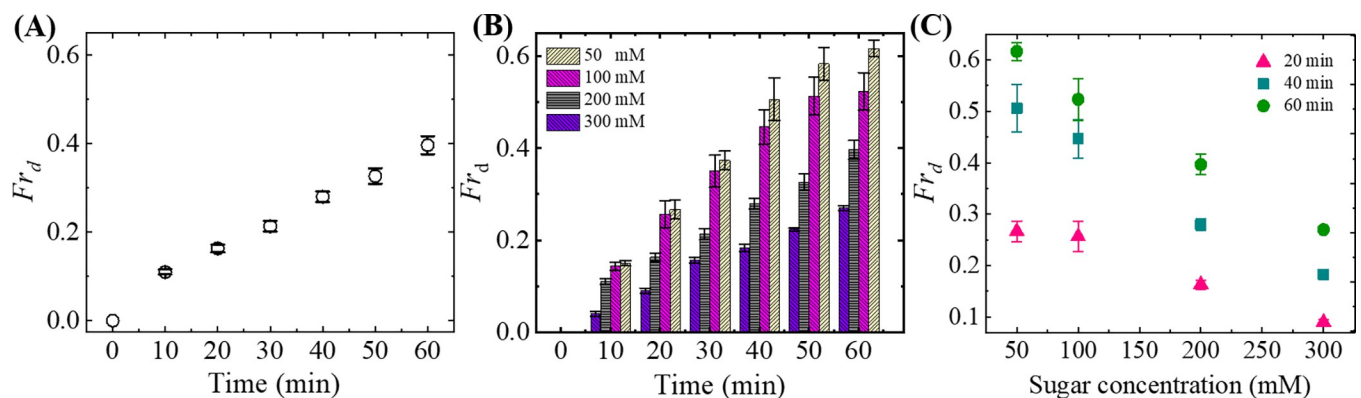
Fig 2. Fraction of deformed 40%DOPG/60%DOPC-GUVs at 3.33 μg/mL. (A) The time course of average Fr_d at 200 mM sugar concentration. (B) Bar chart of Fr_d with time for various sugar concentrations. (C) The sugar concentration-dependent Fr_d at 20, 40 and 60 min. The average values with standard deviations (in B, C, D) were obtained from 3 independent experiments containing 15–20 GUVs in each independent experiment.

https://doi.org/10.1371/journal.pone.0275478.g002

Fr_d obtained were (0.51 ± 0.05), (0.45 ± 0.04), (0.28 ± 0.01) and (0.18 ± 0.01) for $c = 50, 100, 200$ and 300 mM, respectively. So, the average Fr_d decreased with the increase of sugar concentration. This result is clearly depicted in Fig 2(C) where the sugar concentration-dependent average Fr_d at different intervals of time is shown. Therefore, as the sugar concentration in buffer solution increased, the Fr_d decrease, indicating the inhibition of deformation of vesicles with sugar concentration.

3.3 Fraction of deformed 40%DOPG/60%DOPC-GUVs under various NPs concentrations at 50 mM sugar

It is essential to investigate Fr_d at various NPs concentrations, keeping the sugar concentration constant. Here, we present the results from the study of deformation of 40%DOPG/60% DOPC-GUVs under 2.00, 3.33 and 4.67 μg/mL NPs concentrations in GUVs suspension at 50 mM sugar concentration. The bar diagram of time-dependent average Fr_d under various concentrations of NPs is shown in Fig 3(A). The Fr_d increases with time for all concentrations. The NPs concentration-dependent average Fr_d at 20, 40 and 60 min is shown in Fig 3(B). These results clearly indicate that Fr_d increases with increasing NPs concentration in the GUVs suspension. For example, the value of Fr_d at 40 min was (0.27 ± 0.01), (0.28 ± 0.01) and (0.31 ± 0.01) for 2.00, 3.33 and 4.67 μg/mL NPs concentration, respectively. A similar trend to increase the fraction of deformed GUVs was also obtained for other times.

3.4 NPs-induced leakage of calcein from the inside of 40%DOPG/60% DOPC-GUVs and DOPC-GUVs

We investigated the lipid membrane poration of 40%DOPG/60%DOPC-GUVs and DOPC-GUVs induced by 3.33 μg/mL NPs under various concentration of sugar by observing the leakage of fluorescent probe (calcein) from the inside of GUVs. It is to be mentioned here that the Stokes-Einstein radius (R_{SE}) of calcein is 0.74 nm [68]. The dynamic change of a GUV is investigated in Fig 4(A) for 40%DOPG/60%DOPC-GUVs and in Fig 4(B) for DOPC-GUVs due to
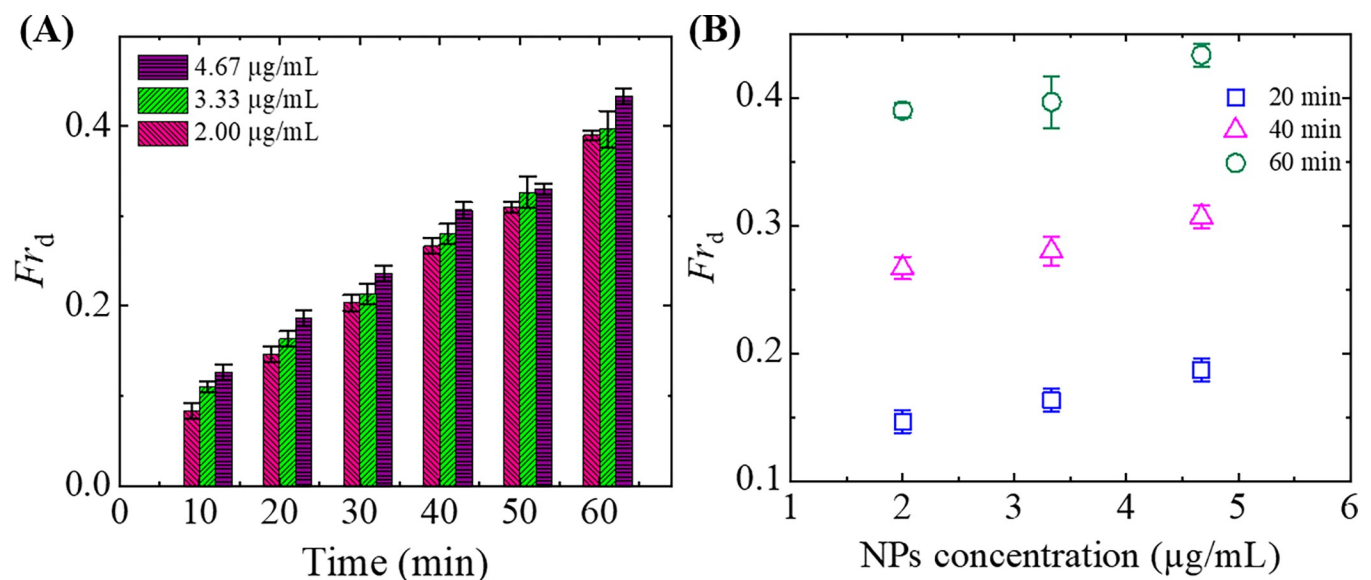
Fig 3. Fraction of deformed 40%DOPG/60%DOPC-GUVs under various NPs concentrations at 50 mM sugar. (A) The bar diagram of Fr_d for 2.00, 3.33 and 4.67 μg/mL NPs. (B) The linear proportionality between NPs concentration and Fr_d at different times. The average values with standard deviations were obtained from 3 independent experiments containing 15–20 GUVs in each independent experiment.
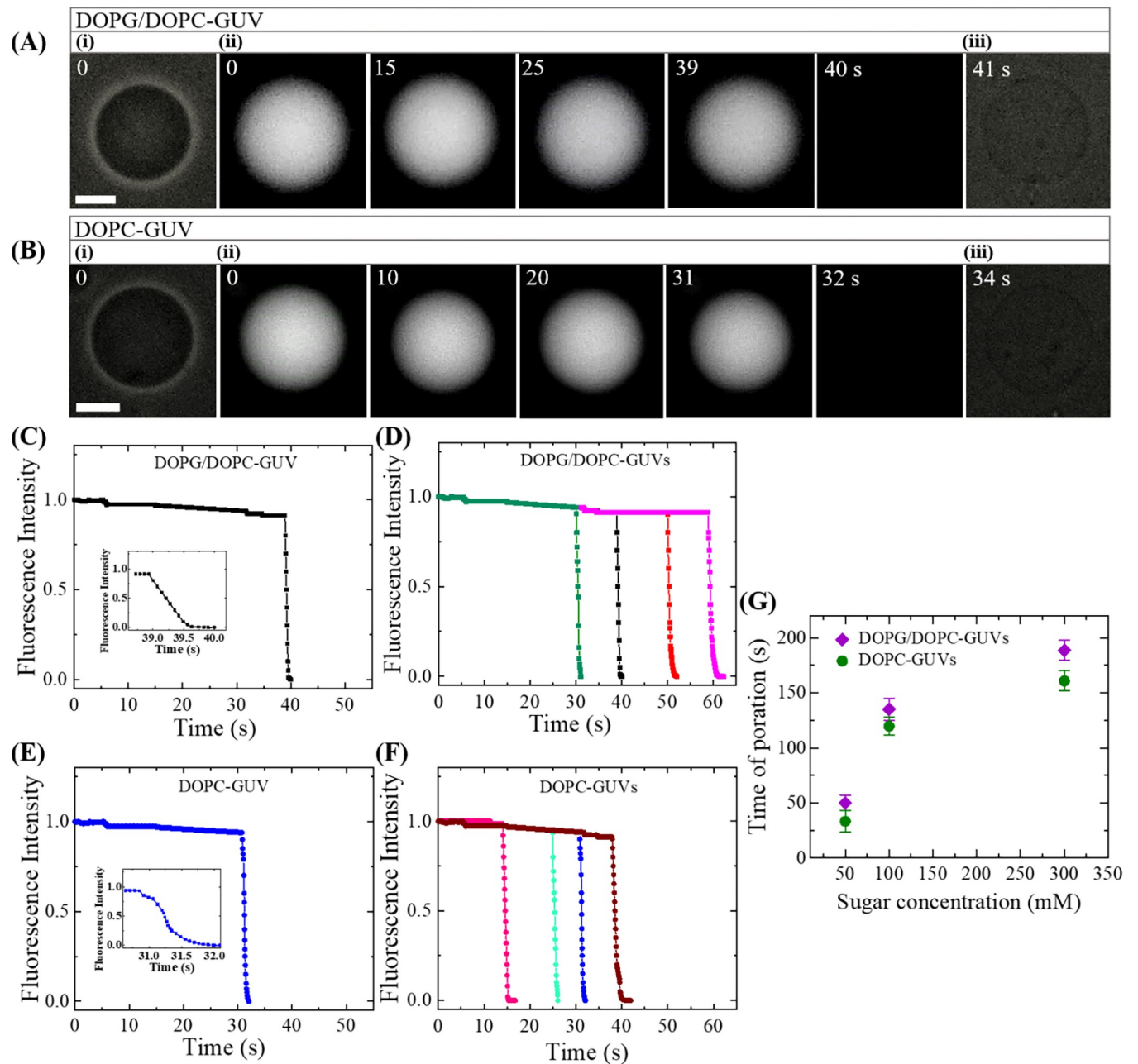
https://doi.org/10.1371/journal.pone.0275478.g003

Fig 4. Pore formation in the membranes of GUVs induced by 3.33 μg/mL NPs. Fluorescence images of (A) 40%DOPG/60%DOPC-GUVs and (B) DOPC-GUVs show the progressive decrease of calcein from inside the GUVs at 50 mM sugar concentration. The numbers on each image show the time in seconds after the NPs are added in the suspension of GUVs. The bar corresponds to 15 μm. Time course of the change of normalized fluorescence intensity of calcein for (C) 40%DOPG/60%DOPC-GUVs and (E) DOPC-GUVs as shown in (A) and (B), respectively. (D, F) Under the same condition corresponding to (C) and (E), the change in normalized fluorescence intensity with time for many GUVs under 50 mM sugar concentration. (G) Sugar concentration-dependent average time of pore formation in 40%DOPG/60%DOPC and DOPC-GUVs.

the interaction of 3.33 μg/mL NPs under 50 mM sugar concentration. Before interacting NPs with the surface of GUVs, it had a high contrast in phase contrast image at 0 s as shown in Fig 4A(i) and 4B(i) due to the difference of refractive index between the internal (sucrose) and external (glucose) solutions of GUVs. The corresponding GUVs in fluorescence microscopy are shown in Fig 4A(ii) and 4B(ii), which showed high concentration of fluorescent material in

the inside of vesicles at this time. During interaction of NPs with GUVs, the fluorescence intensity was almost same until time 39 s (Fig 4A(ii)) and 31 s (Fig 4B(ii)), and then the intensity decreased rapidly with time. The fluorescence intensity became zero at 40 s and 32 s of the corresponding GUVs. After the complete leakage of calcein, the phase contrast images of the corresponding GUVs were spherical and intact with undetectable break as shown in Fig 4A(iii) and 4B(iii). The calcein leakage occurred due to the formation of pores in the membranes induced by NPs. The similar type of the change in fluorescence intensity was also observed for the peptide-induced pore formation in lipid membranes of vesicles [44]. The size of such pores was so small that the vesicles were intact with spherical structure after ejecting the internal calcein. The time-dependent normalized fluorescence intensity of GUVs as shown in Fig 4A and 4B are presented in Fig 4C and 4E, respectively. The intensity was almost same until 39 s (Fig 4C) and 31 s (Fig 4E), followed by a sharp decrease to zero. The sharp decrements occurred within one second and this transformation can be viewed more precisely from the insets of Fig 4C and 4E. The moment of time at which the fluorescence intensity began to rapidly decrease is defined as the time of NPs-induced pore formation in the membranes of GUVs. The fluorescence intensity decreases due to the leakage of calcein from the inside of GUVs to outside. Therefore, there were two states of GUVs due to the interaction of NPs; one was intact state in which the fluorescence intensity was same over time and the another was the pore state in which the fluorescence intensity was decreased rapidly over time and reached to zero. When we conducted similar experiments using many GUVs (n = 15–20) such type of transition from intact state to pore state was also observed. In Fig 4D and 4F, we presented the time-dependent fluorescence intensity of several 40%DOPG/60%DOPC-GUVs and DOPC-GUVs, respectively, under 50 mM sugar concentration. The time of pore formation for several GUVs was not same under the same condition. Thus, the nature of pore formation was stochastic. The reproducibility was checked in several independent experiments using many GUVs. Similar experiments were also done for many GUVs under 100 and 300 mM sugar concentration at 3.33 μg/mL NPs. In those conditions, the pore formation was also in stochastic nature.

The average time of pore formation in stochastic nature under 300 mM sugar concentration was higher than that of 50 and 100 mM sugar concentrations. Fig 4G show the sugar concentration-dependent average time of poration in 40%DOPG/60%DOPC and DOPC-GUVs. In both charged and neutral membranes, the average time for pore formation increased with the increase of sugar concentration in the solution. These investigations clearly indicated that higher sugar concentrations inhibited the pore formation in vesicles.

3.5 Fraction of deformed and pore formed 40%DOPG/60%DOPC and DOPC-GUVs

So far, we have observed two types of phenomena for the interaction of NPs with GUVs; one was deformation, and another was poration. It means that some GUVs became deformed and some GUVs formed pores after interacting NPs. Therefore, it is very important to represent the results using a single graph. The fraction of pore formed GUVs is defined by Fr_p. The time-dependence of both Fr_d and Fr_p is presented in Fig 5A, in which GUVs was interacted with 3.33 μg/mL NPs under 200 mM sugar concentration. While the value of Fr_d increased with time, but the value of Fr_p at first increased with time and then remained steady over time. Hence, the difference in Fr_d and Fr_p until time 20 min was not significant as shown in Fig 5A. This difference increased with time. The maximum difference was obtained at time 50 to 60 min. We repeated the experiment 3 times using many GUVs and obtained the average fractions with standard deviations as shown in Fig 5. Similar experiments for various NPs concentrations under the same sugar concentration were done and those fractions were measured.
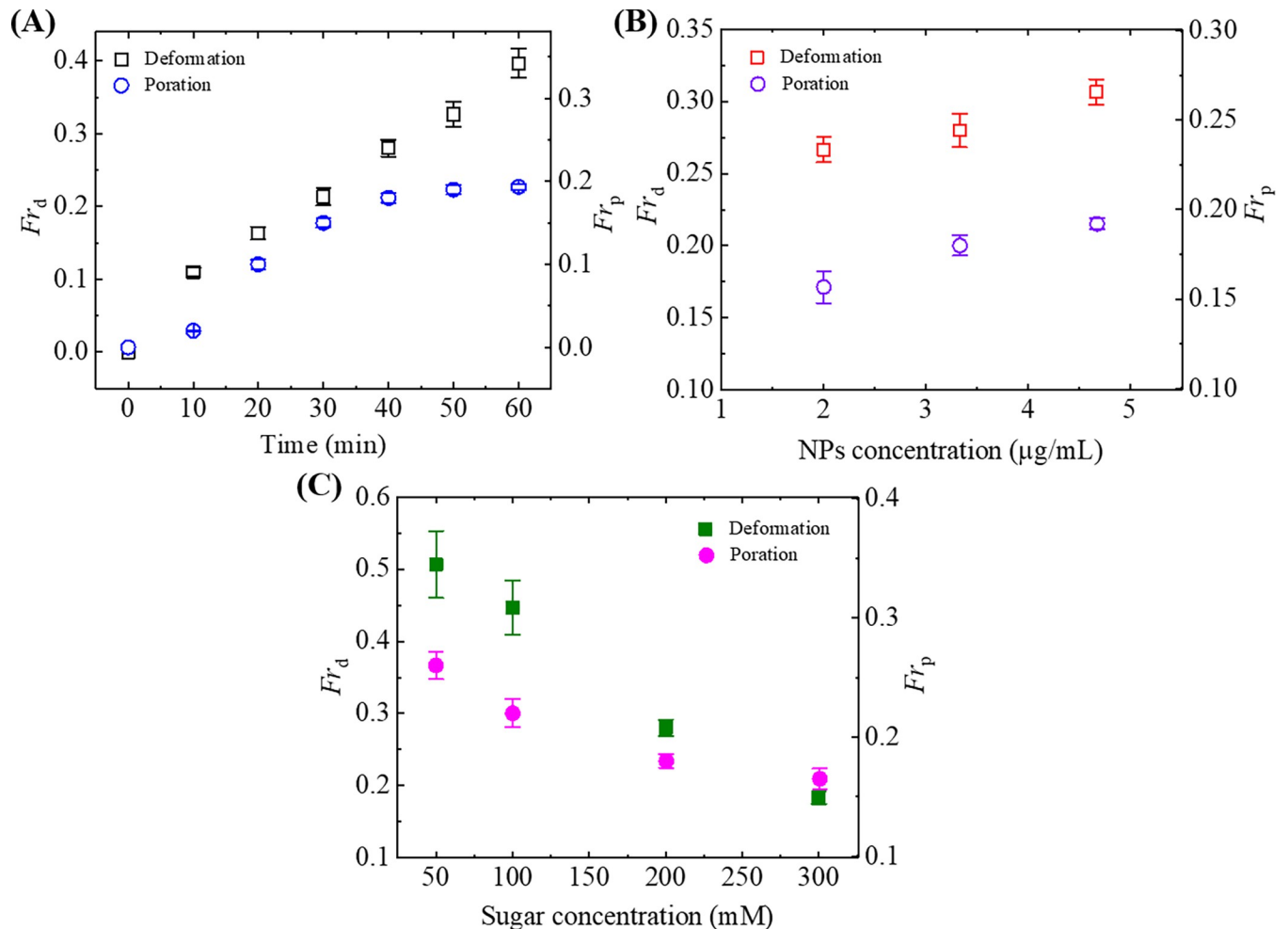
Fig 5. Fraction of deformed and pore formed 40%DOPG/60%DOPC-GUVs. (A) The time-dependent Fr_d and Fr_p under 3.33 μg/mL NPs at 200 mM sugar concentration. (B) The NPs concentration-dependent Fr_d and Fr_p. (C) The sugar concentration-dependent Fr_d and Fr_p using 3.33 μg/mL NPs at 40 min. The average values with standard deviations were obtained from 3 independent experiments containing 15–20 GUVs in each independent experiment.

https://doi.org/10.1371/journal.pone.0275478.g005

The NPs concentration-dependent Fr_d and Fr_p are presented in Fig 5(B). Both the fractions increased with the increase of NPs concentration under 200 mM sugar concentration. However, the rate of increase of those fractions is different. The rate of increase of Fr_d was much higher that of Fr_p at different NPs concentrations. For example, Fr_d was 0.31 ± 0.01 and Fr_p was 0.19 ± 0.01 at 4.67 μg/mL NPs. Hence, the tendency of deformation was higher than the tendency of poration under the same sugar concentration. We performed similar investigations under various concentrations of sugar in buffer solution. Fig 5C shows the sugar concentration-dependent Fr_d and Fr_p using 3.33 μg/mL NPs at 40 min. Both the fractions decreased with sugar concentration. The rate of decrement of Fr_d was slightly higher than the rate of decrement of Fr_p. Hence, the increased sugar concentration in buffer solution reduced these fractions.

To understand the trend of Fr_d and Fr_p, we also calculated those fractions in case of neutral DOPC-GUVs. The time course of Fr_d is depicted in Fig 6A while Fig 6B presents the time course of Fr_p under various sugar concentrations, i.e., c = 50, 100 and 300 mM. Here, both of
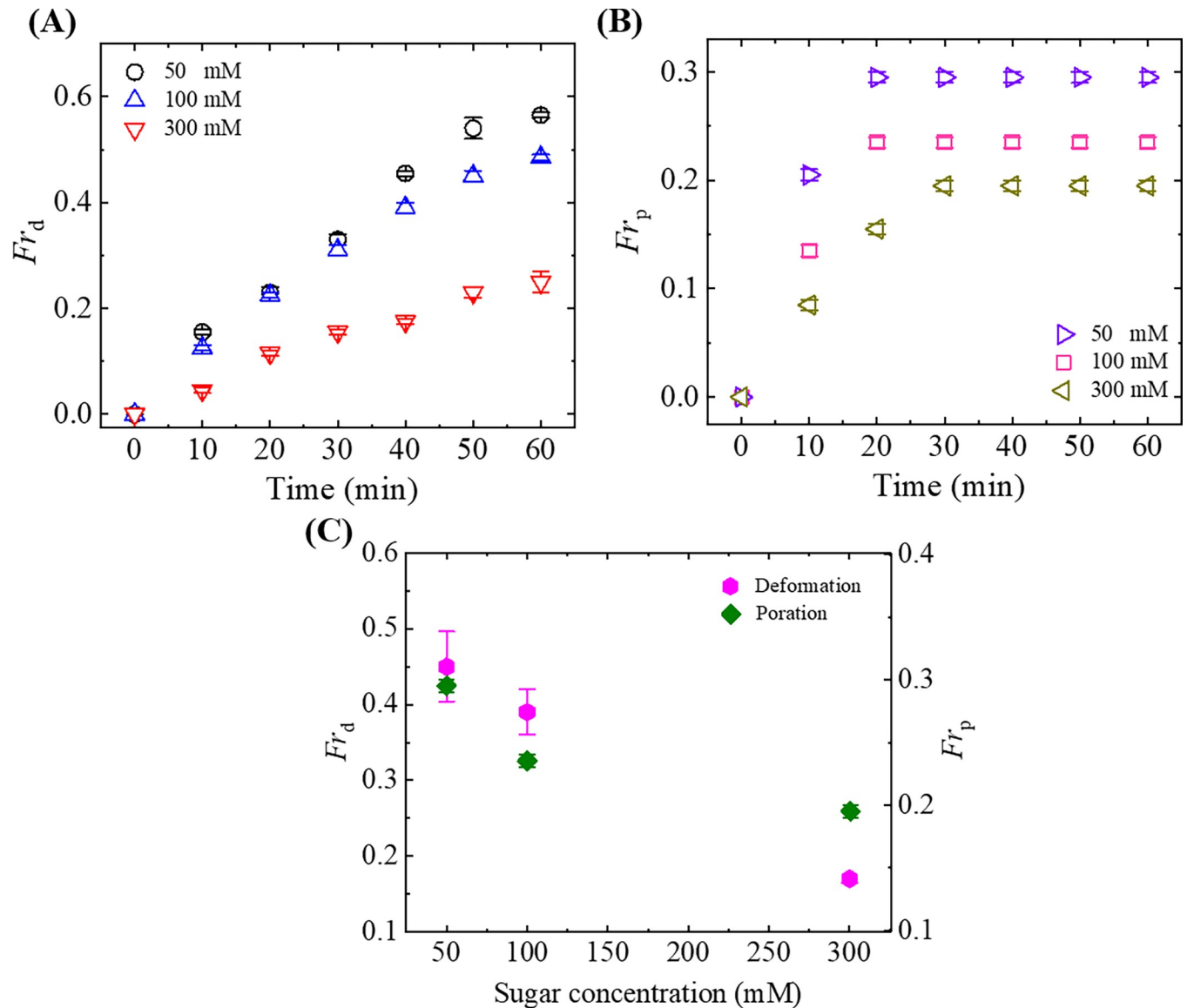
Fig 6. Fraction of deformed and pore formed DOPC-GUVs. The time-dependent (A) Fr_d and (B) Fr_p under 3.33 μg/mL NPs at c = 50, 100 and 300 mM. (C) The sugar concentration-dependent Fr_d and Fr_p using 3.33 μg/mL NPs at 40 min. The average values with standard deviations were obtained from 3 independent experiments containing 15–20 GUVs in each independent experiment.

https://doi.org/10.1371/journal.pone.0275478.g006

those fractions also increased with time for each sugar concentration and Fr_p remained constant from 30 s (Fig 6B). At a certain time, both the Fr_d and Fr_p are higher at lower sugar concentration. For instance, at 50 min, Fr_d were (0.54 ± 0.02), (0.45 ± 0.01) and (0.23 ± 0.01) for c = 50, 100 and 300 mM, respectively, as shown in Fig 6A. On the other hand, Fr_p were (0.30 ± 0.01), (0.24 ± 0.01) and (0.20 ± 0.01) for c = 50, 100 and 300 mM, respectively, at 50 min as shown in Fig 6B. The decrease in Fr_d and Fr_p is evident from Fig 6C where the sugar concentration-dependent Fr_d and Fr_p using 3.33 μg/mL NPs at 40 min is presented. Therefore, it can be said that increase in sugar concentration decreased the deformation and pore formation of both charged and neutral GUVs.
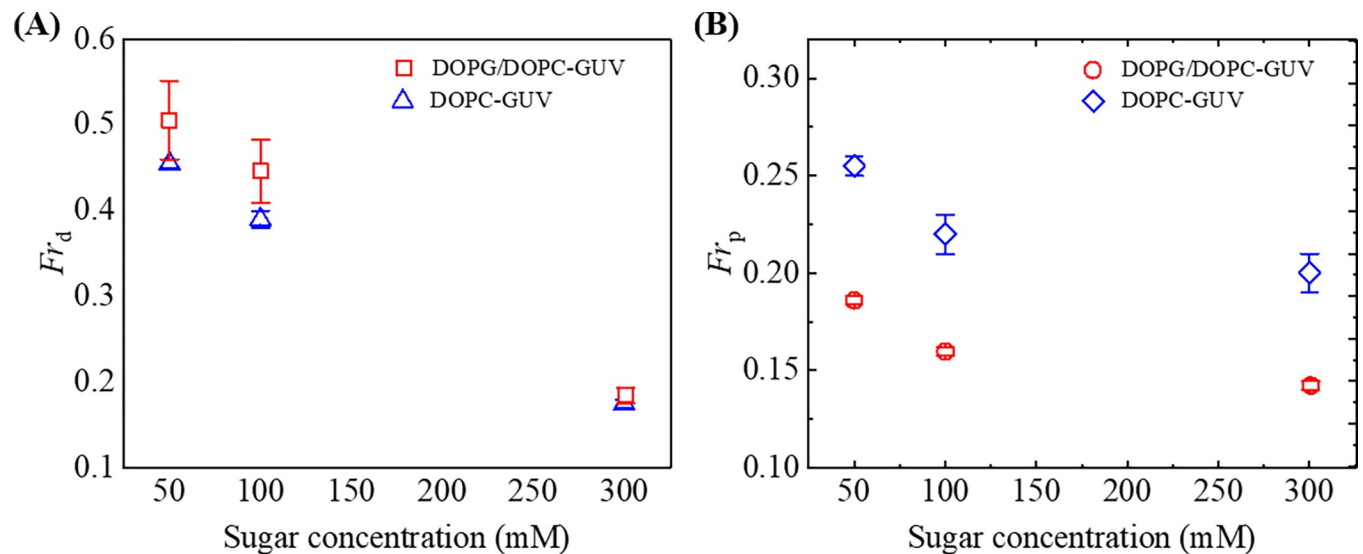
Fig 7. Comparison between the fraction of deformed and pore formed 40%DOPG/60%DOPC-GUVs and DOPC-GUVs under various sugar concentration at 3.33 µg/mL NPs. (A) The sugar concentration-dependent Fr_d for 40%DOPG/60%DOPC-GUVs and DOPC-GUVs at 40 min. (B) The sugar concentration-dependent Fr_p for 40%DOPG/60%DOPC-GUVs and DOPC-GUVs at 40 min. The average values with standard deviations were obtained from 3 independent experiments containing 15–20 GUVs in each independent experiment.

3.6 Comparison of fraction of deformation and poration for 40%DOPG/60%DOPC-GUVs and DOPC-GUVs under various concentrations of sugar

In this section, the comparison between the Fr_d and Fr_p of charged 40%DOPG/60%DOPC-GUVs and neutral DOPC-GUVs under different sugar concentrations is described. Fig 7 shows this comparison very well. For example, at c = 100 mM, Fr_d were (0.45 ± 0.04) and (0.39 ± 0.01), for charged and neutral GUVs, respectively (Fig 7A), and under the same sugar concentration, Fr_p were (0.24 ± 0.01) and (0.22 ± 0.01) for charged and neutral GUVs, respectively (Fig 7B). Both the Fr_d and Fr_p decreased with sugar concentration. The value of Fr_d is higher in charged membrane than the neutral ones, whereas the value of Fr_p is in opposite view. Table 1 depicts the values of Fr_d and Fr_p. From these findings the statement is clear that the probability of deformation is higher for charged membranes compared to neutral ones, whereas the probability of pore formation shows the opposite nature at a fixed sugar condition.

3.7 Different types of deformation of charged and neutral GUVs due to the interaction of 3.33 µg/mL NPs

In section 3.1, we presented the deformation of 40%DOPG/60%DOPC and DOPC-GUVs due to the interaction of 3.33 µg/mL NPs under various sugar concentration. But in our

Table 1. Fraction of deformation and poration in 40%DOPG/60%DOPC-GUVs and DOPC-GUVs for 3.33 µg/mL NPs at 40 min.

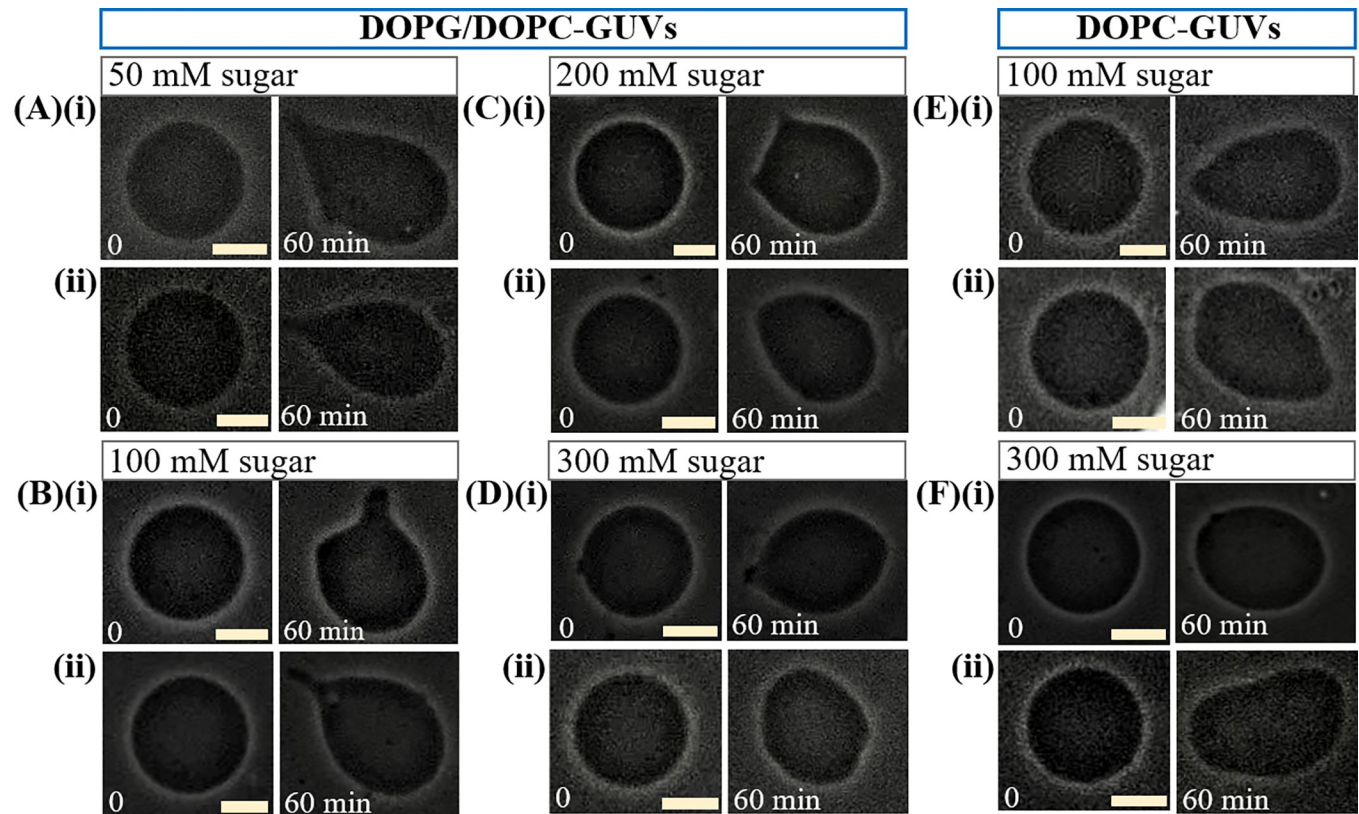| Sugar conc. (mM)	Fraction of deformation		Fraction of poration	
	DOPG/DOPC-GUVs	DOPC-GUVs	DOPG/DOPC-GUVs	DOPC-GUVs
50	0.51 ± 0.05	0.45 ± 0.05	0.26 ± 0.01	0.30 ± 0.01
100	0.45 ± 0.04	0.39 ± 0.03	0.22 ± 0.01	0.24 ± 0.01
200	0.28 ± 0.01	-	0.18 ± 0.01	-
300	0.18 ± 0.01	0.17 ± 0.01	0.17 ± 0.01	0.20 ± 0.01

Fig 8. Different types of deformation of charged and neutral GUVs due to the interaction of 3.33 μg/mL NPs under (A) 50 (B) 100 (C) 200 and (D) 300 mM sugar concentrations. The 'common murre egg-shaped' 40%DOPG/60%DOPC-GUVs in A(i, ii)) and B(ii); 'winnoing fan-shaped' 40%DOPG/60% DOPC-GUVs in B(i) and C(i); 'oval-shaped' 40%DOPG/60%DOPC-GUVs in C(ii) and D(i, ii); 'common murre egg-shaped' DOPC-GUVs in E(i, ii)), and 'Oval-shaped' DOPC-GUVs in F(i, ii). The bar corresponds to 15 μm.

https://doi.org/10.1371/journal.pone.0275478.g008

experiments, we observed different sorts of deformations. Various types of deformation of 40%DOPG/60%DOPC and DOPC-GUVs due to the interaction of 3.33 μg/mL NPs are shown in Fig 8 at 50, 100, 200 and 300 mM sugar concentrations. In all conditions, the GUVs were spherical shape at 0 min (i.e., before interacting NPs with GUVs). After interaction of NPs with membranes, the final shape of GUVs is shown at 60 min. The 'common murre egg-shaped' 40%DOPG/60%DOPC-GUVs are observed in Fig 8A(i, ii)) and 8B(ii) at 50 and 100 mM sugar, respectively. In Fig 8B(i) and 8C(i), 'winnowing fan-shaped' 40%DOPG/60% DOPC-GUVs are observed for 100 and 200 mM sugar concentration, respectively. 'Oval-shaped' 40%DOPG/60%DOPC-GUVs are observed in Fig 8C(ii) and 8D((i, ii) at 200 and 300 mM sugar, respectively. In the similar way, the 'common murre egg-shaped' DOPC-GUVs are observed in Fig 8E(i, ii)), and 'Oval-shaped' DOPC-GUVs are observed in 8F(i, ii) at 100 and 300 mM sugar, respectively.

4. Discussion

The interaction of anionic magnetite NPs with 40%DOPG/60%DOPC and DOPC-GUVs was studied under various sugar concentration in aqueous solution. The GUVs became deformed from their spherical shape upon adoption of NPs into the membrane interface as shown in Fig 1(A) and 1(B). The value of compactness increased with time under various sugar concentrations as shown in Fig 1(C)–1(G). The shape of vesicles is determined by the minimization of

elastic energy of the closed bilayer membrane. According to the 'bilayer-coupling model' [69], the elastic energy of GUVs (W_{el}) is due to only the bending energy of membranes (W_b) as the model did not consider elastic stretching of the monolayers. Hence, the minimum elastic energy is determined by the area difference between the outer monolayer (A^{out}) and the inner monolayer (A^{in}), i.e., $\Delta A = A^{out} - A^{in}$ for a given area A, and a given volume V of the GUVs [70–72]. Later, the shape change (i.e., deformation) of vesicles was well explained by the area-difference-elasticity model (ADE model) [73, 74]. In the ADE model, the area of each monolayer is not fixed to the equilibrium area but can stretch elastically to increase the nonlocal elastic energy of the membranes. The equilibrium shapes of vesicles are assumed to correspond to the minimum of elastic energy of closed bilayer membrane. The elastic energy (W_{el}) is considered as the sum of bending energy of membrane (W_b) and the energy of relative monolayer stretching (W_r) as follows.

$$W_{el} = W_b + W_r$$
$$= \frac{1}{2}k_c \int \left(C_1 + C_2 \right)^2 dA + \frac{1}{2}\frac{k_r}{A_0 h^2}\left(\Delta A - \Delta A_0 \right)^2 \tag{2}$$

where, k_c is the local bending modulus and k_r is the nonlocal bending modulus of membrane. The principal curvatures are C_1, and C_2. Integration is performed over the neutral surface of the bilayer with area A_0. The area difference between the outer and the inner monolayer of the bilayer is denoted by ΔA. The distance between the neutral surfaces of two monolayers is h. The area difference between the two monolayers in the GUVs at equilibrium (i.e., unstretched monolayers) is $\Delta A_0 = A_o^{out} - A_o^{in}$. The difference in area between the external monolayer and the internal monolayer of membranes is $\Delta A = A^{out} - A^{in}$ at stretched state. According to ADE model, the shape of GUVs is determined by the minimization of W_{el} for a given area A, a given volume V, and a given equilibrium (i.e., relaxed) area difference ΔA_0. Under constant volume of GUVs, the deformation of GUVs from spherical to prolate/any other shape is due to $(\Delta A - \Delta A_0)^2$. As the value of this difference increased with time, the deformation (i.e., compactness) of vesicles increased as shown in Fig 1(C)–1(G). The ADE model can also explain the deformation of GUVs with various types of shape as shown in Fig 8. As the sugar concentration increased, the value of average compactness decreased as shown in Fig 1(H). It is reasonably considered that the presence of higher concentration of sugar reduces the mismatch of area between the two layers, induces the decrease of degree of deformation as shown in Fig 1(H). This description is also valid in explaining the results of fraction of deformed GUVs with time and also with sugar concentration as shown in Fig 2. As the NPs concentration increased, the surface pressure in the outer monolayer increased which mismatches more area between the outer monolayer and inner monolayer. The enhanced mismatch area deformed more fraction of GUVs with the increase of NPs concentration as shown in Fig 3. Based on the above discussion, the interaction of NPs with lipid membrane under the influence of sugar concentration is illustrated in Fig 9. We used 50 mM sugar for lower concentration and 300 mM sugar for higher concentration. At lower sugar concentration, the sugar-lipid head groups attractive interaction is attributed to the enthalpy-driven interaction. At higher sugar concentration, sugar-lipid head groups repulsion is attributed to the entropy-driven repulsion. These attractive and repulsive nature of sugar with lipid molecules is also reported by other groups [50, 51]. At a specific NPs concentration, the surface pressure at higher sugar concentrations is lower compared to lower sugar concentrations. The surface pressure changes because of the lower/higher number of bound sugar molecules at the membrane interface at a specific concentration of NPs. The differences in surface pressure at lower/higher sugar concentrations influence the stability of the lipid bilayer. As the surface pressure at lower sugar concentration
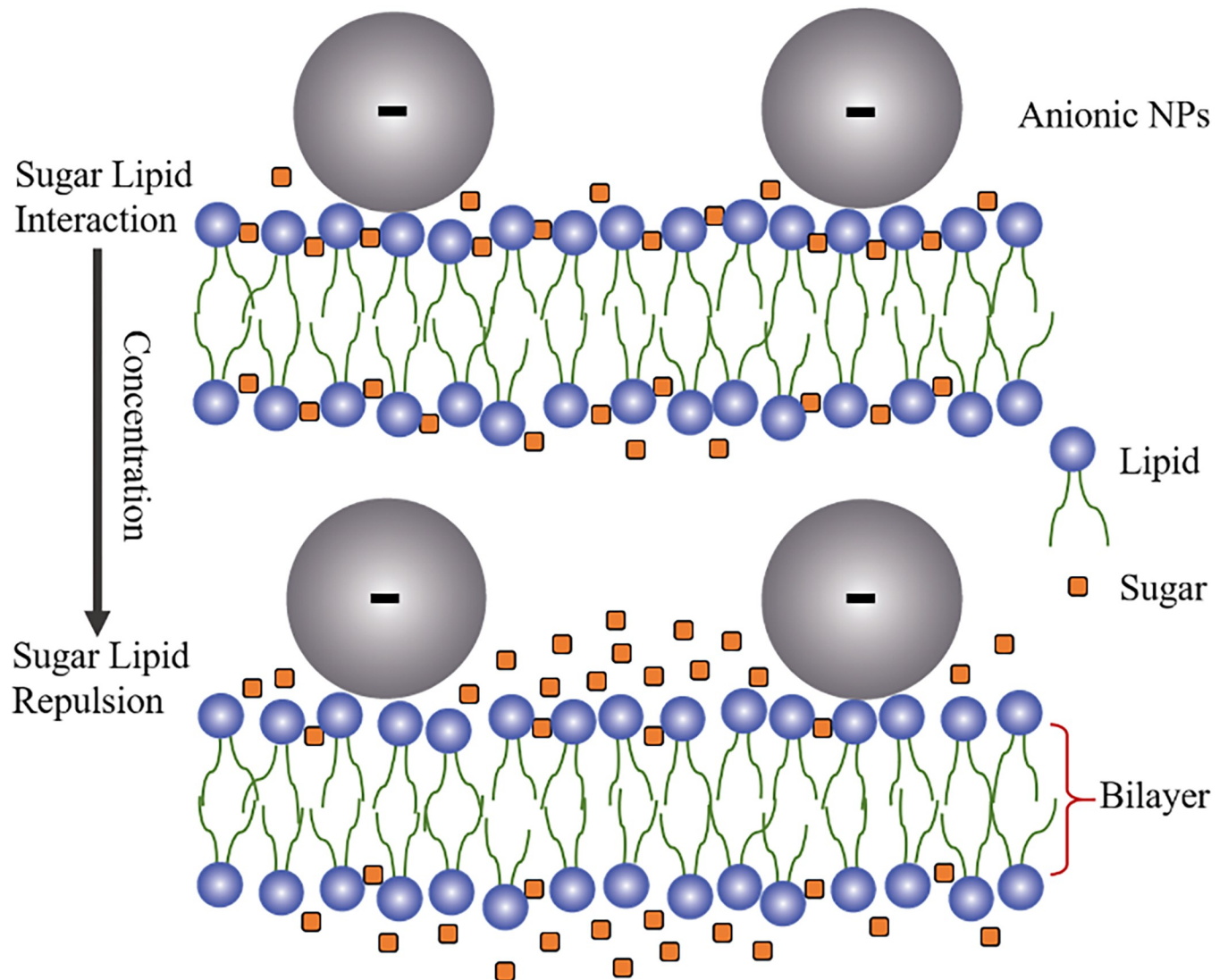
Fig 9. Effects of sugar molecules at lower and higher concentrations in the lipid bilayer for a specific concentration of NPs. The sugar-lipid head groups attractive interaction at lower sugar concentration is attributed to the enthalpy-driven interaction. At higher sugar concentrations, however, the sugar-lipid head groups repulsion is attributed to entropy-driven repulsion. The number density of bound sugar molecules at the interface of lipid molecules in the membrane is higher at lower sugar concentrations than that of higher ones. The sugar molecules at higher sugar concentration are repelled by the lipid molecules.

is higher compared to higher sugar concentration, therefore, the compactness and the possibility of deformation decreased with the increase of sugar concentration (Fig 1H and 2C).

Now we explain the poration of GUVs. Before starting the leakage of calcein from the inside of GUVs, the fluorescent intensity remained constant over time, which is considered as the binding state of NPs with the surface of vesicles. The binding of NPs creates surface pressure on the membrane of vesicles. At 3.33 μg/mL NPs, pre-pores converted to transmembrane pore due to the higher surface pressure. Therefore, these descriptions reasonably explained the NPs-induced poration in GUVs as shown in Fig 4. The stochastic pore formation in several GUVs occurred due to the random initiation of pre-pores in the membranes. Such type of stochastic pore formation was observed in antimicrobial peptide-induced pore formation and tension-induced pore formation in GUVs [75, 76]. Due to the repulsive effect at higher sugar

concentration, the surface pressure is lower which induces the higher energy barrier for transmembrane pore formation. Hence, the possibility of pore formation decreased with the increase of sugar concentration (Figs 5C and 6C).

As the calcein solution was completely leaked out through the pores, the size of pores would be higher than the size of fluorescent probe, i.e., 0.74 nm. According to the investigation shown in Fig 5, we can consider that the pore formation occurred by the irreversible two-state transition. The first state (intact) is the binding of NPs to the external monolayer of the membrane of GUVs and the second state is the state in which pore is created in the membrane. In the two-state model, the membrane surface bends in a toroidal manner resulting in pore formation [77]. The rate constant, k_p is defined as the rate of transition from the intact state to the pore state depending on the energy barrier, U_B given by the Arrhenius equation:

$$k_{\mathrm{p}} = A\exp\left(-\frac{U_{\mathrm{B}}}{k_{\mathrm{B}}T}\right) \qquad (3)$$

where, A is a constant, k_B is the Boltzmann constant and T is the absolute temperature. However, individual events of the two-state transition occur stochastically. If the two-state transition is followed by irreversible pore formation, the fraction of the intact state, $Fr_{\mathrm{intact}}(t)$ can be defined as the fraction of intact GUVs, where no leakage of calcein occurred. After a certain time, there is zero fluorescence intensity found indicating the poration at which calcein leakage occurred. Hence, Fr_p can be expressed as, $1-Fr_{\mathrm{intact}}(t)$. This type of two-state transition occurred stochastically as shown in Fig 4(D) and 4(F).

The dipole ($P^- - N^+$) of DOPC-GUVs has greater attraction to the anionic NPs than to 40% DOPG/60%DOPC-GUVs [30]. The attractive force between NPs and lipid membranes may reach a critical value causing area mismatch between the outer monolayer and inner monolayer faster, resulting in greater fraction of pore formed DOPC-GUVs than the 40%DOPG/ 60%DOPC-GUVs. In contrast, the repulsive force between OH^- and the anionic NPs in 40% DOPG/60%DOPC-GUVs may cause less attraction than the DOPC-GUVs. Hence, area mismatch may increase with longer time in 40%DOPG/60%DOPC-GUVs. This may cause higher fraction of deformed and lower fraction of pore formed 40%DOPG/60%DOPC-GUVs compared to DOPC-GUVs. This situation is consistent with our investigations and is seen clearly in Fig 7.

5. Conclusions

We investigated the anionic magnetite NPs-induced vesicle compactness, vesicle deformation, and lipid membrane poration under various sugar concentrations. The higher concentration of sugar provides additional structural stability to the GUVs, and, consequently, reduces the compactness along with the fraction of deformation and poration. The differences in the NPs effects at lower and higher sugar concentrations are explained by the enthalpy and entropy-driven interactions between sugar molecules and lipid membranes. The area-difference-elasticity model and the classical theory of pore formation, respectively, reasonably explain the deformation and poration of vesicles. The differences in fraction of deformed GUVs and GUVs with pores for DOPG/DOPC and DOPC membranes under various sugar concentrations are explained based on the interaction of NPs with the lipid head structures. The biological implications of sugar molecules as well as their extensive application in biophysical and biochemical research determine the interest in the NPs-induced deformation and poration of cell-sized vesicles under various sugar concentrations. Due to the rapid increase of nano-bio-technology-based research and industry, it is crucial to save ourselves from the exposure of NPs. Adsorption of NPs deforms the cells and also forms pores in cell membranes. Exposure

to NPs affects the cardiovascular and pulmonary activities, resulting in substantial mortality and morbidity. These investigations may contribute to the development of new medical and pharmacological technologies with proper safety measurements.

Author Contributions

Conceptualization: Mohammad Abu Sayem Karal.

Data curation: Sharif Hasan, Mohammad Abu Sayem Karal, Md. Kabir Ahamed.

Formal analysis: Sharif Hasan, Mohammad Abu Sayem Karal, Salma Akter, Marzuk Ahmed, Md. Kabir Ahamed.

Funding acquisition: Mohammad Abu Sayem Karal.

Investigation: Sharif Hasan, Mohammad Abu Sayem Karal, Salma Akter, Shareef Ahammed.

Methodology: Sharif Hasan, Mohammad Abu Sayem Karal, Shareef Ahammed.

Project administration: Mohammad Abu Sayem Karal.

Supervision: Mohammad Abu Sayem Karal.

Validation: Mohammad Abu Sayem Karal, Shareef Ahammed.

Visualization: Sharif Hasan.

Writing – original draft: Mohammad Abu Sayem Karal, Marzuk Ahmed.

Writing – review & editing: Sharif Hasan, Mohammad Abu Sayem Karal, Salma Akter, Marzuk Ahmed, Md. Kabir Ahamed.

References

1. Liu M, Li Q, Liang L, Li J, Wang K, Li J, et al. Real-time visualization of clustering and intracellular transport of gold nanoparticles by correlative imaging. Nat Commun. 2017; 8: 15646. https://doi.org/10.1038/ncomms15646 PMID: 28561031

2. Smith TT, Stephan SB, Moffett HF, McKnight LE, Ji W, Reiman D, et al. In situ programming of leukaemia-specific T cells using synthetic DNA nanocarriers. Nat Nanotechnol. 2017; 12: 813–820. https://doi.org/10.1038/nnano.2017.57 PMID: 28416815

3. Caldorera-Moore ME, Liechty WB, Peppas NA. Responsive theranostic systems: integration of diagnostic imaging agents and responsive controlled release drug delivery carriers. Acc Chem Res. 2011; 44: 1061–1070. https://doi.org/10.1021/ar2001777 PMID: 21932809

4. Mahmoudi M, Sant S, Wang B, Laurent S, Sen T. Superparamagnetic iron oxide nanoparticles (SPIONs): Development, surface modification and applications in chemotherapy. Adv Drug Deliv Rev. 2011; 63: 24–46. https://doi.org/10.1016/j.addr.2010.05.006 PMID: 20685224

5. Farokhzad OC, Langer R. Impact of nanotechnology on drug delivery. ACS Nano. 2009; 3: 16–20. https://doi.org/10.1021/nn900002m PMID: 19206243

6. Gehr P, Zellner R, editors. Biological responses to nanoscale particles: Molecular and cellular aspects and methodological approaches. Springer International Publishing; 2019. https://doi.org/10.1007/978-3-030-12461-8

7. Langer R. Drug delivery and targeting. Nature. 1998; 392: 5–10. PMID: 9579855

8. Alavi M, Karimi N. Ultrasound assisted-phytofabricated Fe3O4 NPs with antioxidant properties and antibacterial effects on growth, biofilm formation, and spreading ability of multidrug resistant bacteria. Artif Cells Nanomedicine Biotechnol. 2019; 47: 2405–2423. https://doi.org/10.1080/21691401.2019.1624560 PMID: 31187647

9. Hajipour MJ, Fromm KM, Akbar Ashkarran A, Jimenez de Aberasturi D, Larramendi IR de, Rojo T, et al. Antibacterial properties of nanoparticles. Trends Biotechnol. 2012; 30: 499–511. https://doi.org/10.1016/j.tibtech.2012.06.004 PMID: 22884769

10. Han X, Jiang X, Guo L, Wang Y, Veeraraghavan VP, Krishna Mohan S, et al. Anticarcinogenic potential of gold nanoparticles synthesized from Trichosanthes kirilowii in colon cancer cells through the

induction of apoptotic pathway. Artif Cells Nanomedicine Biotechnol. 2019; 47: 3577–3584. https://doi.org/10.1080/21691401.2019.1626412 PMID: 31456423

11. Korshed P, Li L, Liu Z, Wang T. The molecular mechanisms of the antibacterial effect of picosecond laser generated silver nanoparticles and their toxicity to human cells. PLOS ONE. 2016; 11: e0160078. https://doi.org/10.1371/journal.pone.0160078 PMID: 27575485

12. Steffy K, Shanthi G, Maroky AS, Selvakumar S. Enhanced antibacterial effects of green synthesized ZnO NPs using Aristolochia indica against Multi-drug resistant bacterial pathogens from Diabetic Foot Ulcer. J Infect Public Health. 2018; 11: 463–471. https://doi.org/10.1016/j.jiph.2017.10.006 PMID: 29150378

13. Upadhyay P, Sarker S, Ghosh A, Gupta P, Das S, Ahir M, et al. Transferrin-decorated thymoquinone-loaded PEG-PLGA nanoparticles exhibit anticarcinogenic effect in non-small cell lung carcinoma via the modulation of miR-34a and miR-16. Biomater Sci. 2019; 7: 4325–4344. https://doi.org/10.1039/c9bm00912d PMID: 31411213

14. Pan Y, Neuss S, Leifert A, Fischler M, Wen F, Simon U, et al. Size-dependent cytotoxicity of gold nano-particles. Small Weinh Bergstr Ger. 2007; 3: 1941–1949. https://doi.org/10.1002/smll.200700378 PMID: 17963284

15. Colvin VL. The potential environmental impact of engineered nanomaterials. Nat Biotechnol. 2003; 21: 1166–1170. https://doi.org/10.1038/nbt875 PMID: 14520401

16. Fischer HC, Chan WCW. Nanotoxicity: the growing need for in vivo study. Curr Opin Biotechnol. 2007; 18: 565–571. https://doi.org/10.1016/j.copbio.2007.11.008 PMID: 18160274

17. Lewinski N, Colvin V, Drezek R. Cytotoxicity of nanoparticles. Small Weinh Bergstr Ger. 2008; 4: 26–49. https://doi.org/10.1002/smll.200700595 PMID: 18165959

18. Nel AE, Mädler L, Velegol D, Xia T, Hoek EMV, Somasundaran P, et al. Understanding biophysico-chemical interactions at the nano-bio interface. Nat Mater. 2009; 8: 543–557. https://doi.org/10.1038/nmat2442 PMID: 19525947

19. Fadeel B, Garcia-Bennett AE. Better safe than sorry: Understanding the toxicological properties of inor-ganic nanoparticles manufactured for biomedical applications. Adv Drug Deliv Rev. 2010; 62: 362–374. https://doi.org/10.1016/j.addr.2009.11.008 PMID: 19900497

20. Buzea C, Pacheco II, Robbie K. Nanomaterials and nanoparticles: Sources and toxicity. Biointer-phases. 2007; 2: MR17–MR71. https://doi.org/10.1116/1.2815690 PMID: 20419892

21. Kendall M, Lynch I. Long-term monitoring for nanomedicine implants and drugs. Nat Nanotechnol. 2016; 11: 206–210. https://doi.org/10.1038/nnano.2015.341 PMID: 26936811

22. Souza VGL, Fernando AL. Nanoparticles in food packaging: Biodegradability and potential migration to food—A review. Food Packag Shelf Life. 2016; 8: 63–70. https://doi.org/10.1016/j.fpsl.2016.04.001

23. Atmosphere Nel A. Air pollution-related illness: effects of particles. Science. 2005; 308: 804–806. https://doi.org/10.1126/science.1108752 PMID: 15879201

24. Chan JKW, Fanucchi MV, Anderson DS, Abid AD, Wallis CD, Dickinson DA, et al. Susceptibility to inhaled flame-generated ultrafine soot in neonatal and adult rat lungs. Toxicol Sci Off J Soc Toxicol. 2011; 124: 472–486. https://doi.org/10.1093/toxsci/kfr233 PMID: 21914721

25. Chithrani BD, Ghazani AA, Chan WCW. Determining the size and shape dependence of gold nanoparti-cle uptake into mammalian cells. Nano Lett. 2006; 6: 662–668. https://doi.org/10.1021/nl052396o PMID: 16608261

26. Rejman J, Oberle V, Zuhorn IS, Hoekstra D. Size-dependent internalization of particles via the path-ways of clathrin- and caveolae-mediated endocytosis. Biochem J. 2004; 377: 159–169. https://doi.org/10.1042/BJ20031253 PMID: 14505488

27. Wang Q, Sun Y, Zhang Z, Duan Y. Targeted polymeric therapeutic nanoparticles: Design and interac-tions with hepatocellular carcinoma. Biomaterials. 2015; 56: 229–240. https://doi.org/10.1016/j.biomaterials.2015.03.050 PMID: 25934295

28. Maher BA, Ahmed IAM, Karloukovski V, MacLaren DA, Foulds PG, Allsop D, et al. Magnetite pollution nanoparticles in the human brain. Proc Natl Acad Sci. 2016; 113: 10797–10801. https://doi.org/10.1073/pnas.1605941113 PMID: 27601646

29. Plascencia-Villa G, Ponce A, Collingwood JF, Arellano-Jiménez MJ, Zhu X, Rogers JT, et al. High-reso-lution analytical imaging and electron holography of magnetite particles in amyloid cores of Alzheimer's disease. Sci Rep. 2016; 6: 24873. https://doi.org/10.1038/srep24873 PMID: 27121137

30. Karal MAS, Ahammed S, Levadny V, Belaya M, Ahamed MdK, Ahmed M, et al. Deformation and pora-tion of giant unilamellar vesicles induced by anionic nanoparticles. Chem Phys Lipids. 2020; 104916. https://doi.org/10.1016/j.chemphyslip.2020.104916 PMID: 32407734

31. Bohnert HJ, Nelson DE, Jensen RG. Adaptations to environmental stresses. Plant Cell. 1995; 7: 1099–1111. https://doi.org/10.1105/tpc.7.7.1099 PMID: 12242400

32. Bray EA. Plant responses to water deficit. Trends Plant Sci. 1997; 2: 48–54. https://doi.org/10.1016/S1360-1385(97)82562-9

33. Yancey PH, Clark ME, Hand SC, Bowlus RD, Somero GN. Living with water stress: evolution of osmo-lyte systems. Science. 1982; 217: 1214–1222. https://doi.org/10.1126/science.7112124 PMID: 7112124

34. Crowe LM, Reid DS, Crowe JH. Is trehalose special for preserving dry biomaterials? Biophys J. 1996; 71: 2087–2093. https://doi.org/10.1016/S0006-3495(96)79407-9 PMID: 8889183

35. Luzardo M del C, Amalfa F, Nuñez AM, Díaz S, Biondi de Lopez AC, Disalvo EA. Effect of Trehalose and sucrose on the hydration and dipole potential of lipid bilayers. Biophys J. 2000; 78: 2452–2458. https://doi.org/10.1016/s0006-3495(00)76789-0 PMID: 10777741

36. Döbereiner H-G, Selchow O, Lipowsky R. Spontaneous curvature of fluid vesicles induced by trans-bilayer sugar asymmetry. Eur Biophys J. 1999; 28: 174–178. https://doi.org/10.1007/s002490050197

37. Vitkova V, Mitkova D, Antonova K, Popkirov G, Dimova R. Sucrose solutions alter the electric capaci-tance and dielectric permittivity of lipid bilayers. Colloids Surf Physicochem Eng Asp. 2018; 557: 51–57. https://doi.org/10.1016/j.colsurfa.2018.05.011

38. Genova J, Zheliaskova A, Mitov MD. The influence of sucrose on the elasticity of SOPC lipid membrane studied by the analysis of thermally induced shape fluctuations. Colloids Surf Physicochem Eng Asp. 2006; 282–283: 420–422. https://doi.org/10.1016/j.colsurfa.2005.11.065

39. Nagle JF, Jablin MS, Tristram-Nagle S, Akabori K. What are the true values of the bending modulus of simple lipid bilayers? Chem Phys Lipids. 2015; 185: 3–10. https://doi.org/10.1016/j.chemphyslip.2014.04.003 PMID: 24746555

40. Vitkova V, Genova J, Mitov MD, Bivas I. Sugars in the aqueous phase change the mechanical proper-ties of lipid mono- and bilayers. Mol Cryst Liq Cryst. 2006; 449: 95–106. https://doi.org/10.1080/15421400600582515

41. Sarkar MK, Karal MAS, Levadny V, Belaya M, Ahmed M, Ahamed MK, et al. Effects of sugar concentra-tion on the electroporation, size distribution and average size of charged giant unilamellar vesicles. Eur Biophys J. 2022; 51: 401–412. https://doi.org/10.1007/s00249-022-01607-y PMID: 35716178

42. Islam MZ, Alam JM, Tamba Y, Karal MAS, Yamazaki M. The single GUV method for revealing the func-tions of antimicrobial, pore-forming toxin, and cell-penetrating peptides or proteins. Phys Chem Chem Phys. 2014; 16: 15752–15767. https://doi.org/10.1039/c4cp00717d PMID: 24965206

43. Karal MAS, Islam MK, Mahbub ZB. Study of molecular transport through a single nanopore in the mem-brane of a giant unilamellar vesicle using COMSOL simulation. Eur Biophys J. 2020; 49: 59–69. https://doi.org/10.1007/s00249-019-01412-0 PMID: 31796980

44. Karal MAS, Alam J, Takahashi T, Levadny V, Yamazaki M. Stretch-activated pore of the antimicrobial peptide, magainin 2. Langmuir. 2015; 31: 3391–3401. https://doi.org/10.1021/la503318z PMID: 25746858

45. Wang B, Zhang L, Bae SC, Granick S. Nanoparticle-induced surface reconstruction of phospholipid membranes. Proc Natl Acad Sci. 2008; 105: 18171–18175. https://doi.org/10.1073/pnas.0807296105 PMID: 19011086

46. Dimova R, Riske KA, Aranda S, Bezlyepkina N, Knorr RL, Lipowsky R. Giant vesicles in electric fields. Soft Matter. 2007; 3: 817. https://doi.org/10.1039/b703580b PMID: 32900072

47. Karal MAS, Ahamed MK, Ahmed M, Mahbub ZB. Recent developments in the kinetics of ruptures of giant vesicles under constant tension. RSC Adv. 2021; 11: 29598–29619. https://doi.org/10.1039/d1ra04647k PMID: 35479542

48. Vereyken IJ, Chupin V, Demel RA, Smeekens SCM, De Kruijff B. Fructans insert between the head-groups of phospholipids. Biochim Biophys Acta BBA—Biomembr. 2001; 1510: 307–320. https://doi.org/10.1016/s0005-2736(00)00363-1 PMID: 11342168

49. Demel RA, Dorrepaal E, Ebskamp MJM, Smeekens JCM, de Kruijff B. Fructans interact strongly with model membranes. Biochim Biophys Acta BBA—Biomembr. 1998; 1375: 36–42. https://doi.org/10.1016/s0005-2736(98)00138-2 PMID: 9767096

50. Dhaliwal A, Khondker A, Alsop R, Rheinstädter MC. Glucose can protect membranes against dehydra-tion damage by inducing a glassy membrane state at low hydrations. Membranes. 2019; 9: 15. https://doi.org/10.3390/membranes9010015 PMID: 30650602

51. Andersen HD, Wang C, Arleth L, Peters GH, Westh P. Reconciliation of opposing views on membrane-sugar interactions. Proc Natl Acad Sci U S A. 2011; 108: 1874–1878. https://doi.org/10.1073/pnas.1012516108 PMID: 21245346

52. Hillaireau H, Couvreur P. Nanocarriers' entry into the cell: relevance to drug delivery. Cell Mol Life Sci. 2009; 66: 2873–2896. https://doi.org/10.1007/s00018-009-0053-z PMID: 19499185

53. Rothen-Rutishauser BM, Schürch S, Haenni B, Kapp N, Gehr P. Interaction of fine particles and nano-particles with red blood cells visualized with advanced microscopic techniques. Environ Sci Technol. 2006; 40: 4353–4359. https://doi.org/10.1021/es0522635 PMID: 16903270

54. West B, Brown FLH, Schmid F. Membrane-protein interactions in a generic coarse-grained model for lipid bilayers. Biophys J. 2009; 96: 101–115. https://doi.org/10.1529/biophysj.108.138677 PMID: 18835907

55. Aranda-Espinoza H, Berman A, Dan N, Pincus P, Safran S. Interaction between inclusions embedded in membranes. Biophys J. 1996; 71: 648–656. https://doi.org/10.1016/S0006-3495(96)79265-2 PMID: 8842204

56. Dan N, Berman A, Pincus P, A. Safran S. Membrane-induced interactions between inclusions. J Phys II. 1994; 4: 1713–1725. https://doi.org/10.1051/jp2:1994227

57. Schmidt U, Guigas G, Weiss M. Cluster formation of transmembrane proteins due to hydrophobic mis-matching. Phys Rev Lett. 2008; 101: 128104. https://doi.org/10.1103/PhysRevLett.101.128104 PMID: 18851417

58. Yu Y, Granick S. Pearling of lipid vesicles induced by nanoparticles. J Am Chem Soc. 2009; 131: 14158–14159. https://doi.org/10.1021/ja905900h PMID: 19775107

59. Contini C, Schneemilch M, Gaisford S, Quirke N. Nanoparticle–membrane interactions. J Exp Nanosci. 2018; 13: 62–81. https://doi.org/10.1080/17458080.2017.1413253

60. Laurencin M, Georgelin T, Malezieux B, Siaugue J-M, Ménager C. Interactions between giant unilamel-lar vesicles and charged core−shell magnetic nanoparticles. Langmuir. 2010; 26: 16025–16030. https://doi.org/10.1021/la1023746 PMID: 20866045

61. Li S, Malmstadt N. Deformation and poration of lipid bilayer membranes by cationic nanoparticles. Soft Matter. 2013; 9: 4969–4976. https://doi.org/10.1039/C3SM27578G

62. Zaman MM, Karal MAS, Khan MNI, Tareq ARM, Ahammed S, Akter M, et al. Eco-friendly synthesis of Fe3O4 Nanoparticles Based on Natural Stabilizers and Their Antibacterial Applications. ChemistrySe-lect. 2019; 4: 7824–7831. https://doi.org/10.1002/slct.201901594

63. Walde P, Cosentino K, Engel H, Stano P. Giant vesicles: preparations and applications. Chembiochem Eur J Chem Biol. 2010; 11: 848–865. https://doi.org/10.1002/cbic.201000010 PMID: 20336703

64. Reeves JP, Dowben RM. Formation and properties of thin-walled phospholipid vesicles. J Cell Physiol. 1969; 73: 49–60. https://doi.org/10.1002/jcp.1040730108 PMID: 5765779

65. Tamba Y, Terashima H, Yamazaki M. A membrane filtering method for the purification of giant unilamel-lar vesicles. Chem Phys Lipids. 2011; 164: 351–358. https://doi.org/10.1016/j.chemphyslip.2011.04.003 PMID: 21524642

66. Karal MAS, Rahman M, Ahamed MK, Shibly SUA, Ahmed M, Shakil MM. Low cost non-electromechani-cal technique for the purification of giant unilamellar vesicles. Eur Biophys J. 2019; 48:349–359. https://doi.org/10.1007/s00249-019-01363-6 PMID: 30918998

67. Fenster A. Handbook of medical imaging, processing and analysis: Edited by Isaac N. Bankman, PhD, Academic Press, 2000, ISBN 0-12-077790-8, 901 pp. Ultrasound Med Biol. 2001; 27: 727. https://doi.org/10.1016/S0301-5629(01)00360-X

68. Tamba Y, Ariyama H, Levadny V, Yamazaki M. Kinetic pathway of antimicrobial peptide magainin 2-induced pore formation in lipid membranes. J Phys Chem B. 2010; 114: 12018–12026. https://doi.org/10.1021/jp104527y PMID: 20799752

69. Käs J, Sackmann E. Shape transitions and shape stability of giant phospholipid vesicles in pure water induced by area-to-volume changes. Biophys J. 1991; 60: 825–844. https://doi.org/10.1016/S0006-3495(91)82117-8 PMID: 1742455

70. Iglic A, Kralj-Iglic V, Majhenc J. Cylindrical shapes of closed lipid bilayer structures correspond to an extreme area difference between the two monolayers of the bilayer. J Biomech. 1999; 32: 1343–1347. https://doi.org/10.1016/s0021-9290(99)00136-0 PMID: 10569713

71. Seifert U, Berndl K, Lipowsky R. Shape transformations of vesicles: Phase diagram for spontaneous-curvature and bilayer-coupling models. Phys Rev A. 1991; 44: 1182–1202. https://doi.org/10.1103/physreva.44.1182 PMID: 9906067

72. Svetina S, Žekš B. Membrane bending energy and shape determination of phospholipid vesicles and red blood cells. Eur Biophys J. 1989; 17: 101–111. https://doi.org/10.1007/BF00257107 PMID: 2766997

73. Heinrich V, Svetina S, Žekš B. Nonaxisymmetric vesicle shapes in a generalized bilayer-couple model and the transition between oblate and prolate axisymmetric shapes. Phys Rev E. 1993; 48: 3112–3123. https://doi.org/10.1103/PhysRevE.48.3112 PMID: 9960950

74. Miao L, Seifert U, Wortis M, Döbereiner H-G. Budding transitions of fluid-bilayer vesicles: The effect of area-difference elasticity. Phys Rev E. 1994; 49: 5389–5407. https://doi.org/10.1103/physreve.49.5389 PMID: 9961866

75. Ahamed MK, Karal MAS, Ahmed M, Ahammed S. Kinetics of irreversible pore formation under constant electrical tension in giant unilamellar vesicles. Eur Biophys J. 2020; 49: 371–381. https://doi.org/10.1007/s00249-020-01440-1 PMID: 32494845

76. Tamba Y, Yamazaki M. Magainin 2-induced pore formation in the lipid membranes depends on its concentration in the membrane interface. J Phys Chem B. 2009; 113: 4846–4852. https://doi.org/10.1021/jp8109622 PMID: 19267489

77. Tamba Y, Yamazaki M. Single giant unilamellar vesicle method reveals effect of antimicrobial peptide magainin 2 on membrane permeability. Biochemistry. 2005; 44: 15823–15833. https://doi.org/10.1021/bi051684w PMID: 16313185